Available online at www.sciencedirect.com
ScienceDirect
Acta Materialia 55 (2007) 5581–5591
Acta MATERIALIA
www.elsevier.com/locate/actamat

Processing and properties of sintered reaction-bonded silicon nitride with Y_2O_3–$MgSiN_2$: Effects of Si powder and Li_2O addition

Xinwen Zhu [a,*], Yoshio Sakka [a], You Zhou [b], Kiyoshi Hirao [b]

[a] *Fine Particle Processing Group, Nano Ceramics Center, National Institute for Materials Science (NIMS), 1-2-1 Sengen, Tsukuba, Ibaraki 305-0047, Japan*
[b] *Advanced Manufacturing Research Institute, National Institute of Advanced Industrial Science and Technology (AIST), Shimo-shidami, Moriyama-ku, Nagoya 463-8560, Japan*

Received 19 April 2007; received in revised form 15 June 2007; accepted 15 June 2007
Available online 2 August 2007

Abstract

The effects of Si powder and Li_2O addition on the processing, thermal conductivity and mechanical properties of sintered reaction-bonded silicon nitride (SRBSN) with Y_2O_3–$MgSiN_2$ sintering aids were studied. Addition of Li_2O provides a less-viscous liquid phase that results in a more uniform and finer pore structure in RBSN with the coarser Si powders, but the pore structure plays a less important role in the densification of RBSN. The thermal conductivity of SRBSN without porosity decreases with increased Al impurity content and also decreases with the Li_2O addition regardless of the Si purity. The impurest coarse Si powder produces the lowest thermal conductivity (93 W m^{-1} K^{-1}) but the highest four-point bending strength (~700 MPa) and a higher fracture toughness (~10 MPa $m^{1/2}$). However, the purer fine Si powder produces the highest thermal conductivity (119 W m^{-1} K^{-1}) and highest toughness (~11 MPa $m^{1/2}$) but the lowest strength (~500 MPa).

Keywords: Sintered reaction-bonded silicon nitride; Nucleation and growth; Fracture; Toughness; Thermal conductivity

1. Introduction

Silicon nitride (Si_3N_4) is an important structural ceramic material suitable for various applications such as automotive engine parts, industrial wear parts, cutting tools, ceramic armor, etc., due to its excellent mechanical properties, good resistance to thermal shock and chemical attack, excellent creep resistance, and good tribological and wear properties [1]. The recent discovery that this material also has high thermal conductivity makes Si_3N_4 a promising candidate material for integrated circuit (IC) substrates and heat sinks [2–4]. However, cost is always the major barrier to commercial applications of Si_3N_4 ceramics. Sintered reaction-bonded silicon nitride (SRBSN) is a well-known, cost-effective Si_3N_4 ceramic material because of the low cost of Si raw powder, the machinability of the RBSN body and the lower sintering shrinkage [5,6]. The development of SRBSN, which combines high thermal conductivity with good mechanical properties, will undoubtedly help expand the industrial applications of Si_3N_4 components as both structural and functional materials.

Our previous work reported that the improvement in the thermal conductivity of SRBSN could be achieved by using coarse Si powders with lower amounts of oxygen and aluminum impurities [7], which are the two major impurities detrimental to the thermal conductivity of β-Si_3N_4 because of phonon scattering [8,9]. Although the use of purer coarse Si powders is beneficial for enhancing the thermal conductivity, the increase in Si particle size tends to retard densification of RBSN for two major reasons: (i) the increased grain size of Si_3N_4 products and (ii) the reduced amount of liquid phase [10,11]. However, complete densification is necessary to enhance the thermal conductivity and

* Corresponding author. Tel.: +81 29 859 2463; fax: +81 29 859 2401.
E-mail address: Zhu.xinwen@nims.go.jp (X. Zhu).

1359-6454/$30.00
doi:10.1016/j.actamat.2007.06.014

mechanical properties of ceramics. To achieve complete densification of SRBSN using coarse Si powders of several micrometers, or even a few tenths of a micrometer, higher amounts of sintering aids are often required [11]. However, this tends to lower the thermal conductivity because of the increased amount of secondary phases, which show thermal conductivities ($\sim$1 W m^{-1} K^{-1} for the amorphous phase and $\sim$10 W m^{-1} K^{-1} for the crystalline phase) much lower than that of pure β-Si_3N_4 crystals (*a*-axis: $\sim$180 W m^{-1} K^{-1}; *c*-axis: $\sim$450 W m^{-1} K^{-1}) [12]. To minimize the negative effect of residual secondary phases on the thermal conductivity of AlN ceramics, Watari et al. [13] proposed a processing strategy that used an additional disappearing sintering aid, which provides a low-viscosity liquid phase to promote densification during the initial and middle sintering but can be removed in gaseous form from the samples during the final stage of sintering. Moreover, they reported that Li_2O can serve as this kind of disappearing aid, as it can be removed in gaseous form at temperatures below 1600 °C, due to its high vapor pressure (10^{-1} Pa at 1300 °C, 1 Pa at 1500 °C and 10 Pa at 1600 °C) [13]. The concurrent use of Li_2O with Y_2O_3 and CaO resulted not only in low-temperature (1600 °C) sintering but also in improvement in the thermal conductivity of AlN ceramics, due to the pore elimination, AlN lattice purification and grain-boundary phase evaporation [13,14].

Matovic et al. [15,16] reported that the use of Li_2O together with Y_2O_3 is also effective for achieving the low-temperature sintering of Si_3N_4 at 1600 °C. They showed that the rapid evaporation of Li_2O starts at 1500 °C and the Li_2O concentration is reduced from $\sim$1.75 to $\sim$0.08 wt.% after sintering for 8 h at 1500 °C, suggesting that the Li_2O liquid phase is only transient. Thus, it is expected that the Li_2O addition together with Y_2O_3 and $MgSiN_2$ would promote not only the post-sintering of RBSN but also the thermal conductivity of SRBSN with coarse Si powders. Similar to Mg and Y, Li is believed to dissolve in Si_3N_4 only in the presence of both Al and O [17,18]. The same authors also showed that Li_2O evaporation is significantly suppressed in the case of the $LiAlSiO_4$ additive in comparison with the $LiYO_2$ additive [19]. This means that the effect of Li_2O addition on the thermal conductivity of SRBSN probably depends on the Al impurity in the Si powders.

The present work is intended to study the effects of Si powder type and Li_2O addition on the processing, thermal conductivity and mechanical properties of SRBSN. A mixture of Y_2O_3 and $MgSiN_2$ was chosen as the primary additive composition for the following two reasons: (i) to enhance the thermal conductivity [20], and (ii) to study the effect of Li_2O addition on the pore structure development in RBSN and the post-sintering behavior of RBSN [21]. Three types of Si powders that revealed a significant difference in the Al impurity were chosen. Two of them were coarse and the other one was fine. The nitriding process was studied in terms of the degree of nitridation, density, α/β phase ratio, crystalline secondary phase and microstructure. The post-sintering process was studied in terms of the densification, weight loss, crystalline secondary phases and microstructure. The thermal conductivity and mechanical properties of the resultant SRBSN materials were evaluated.

2. Experimental procedure

Three types of commercial Si powders (Yamayishi Metal Co. Ltd., Tokyo, Japan) were used in this investigation. The characteristics of the as-received Si powders are shown in Table 1. According to the manufacturer's information, powder B was prepared from powder A using a milling process. The morphology of the powders was observed by scanning electron microscopy (SEM) (JSM-5600, JEOL Ltd., Tokyo, Japan). The oxygen contents were measured by an oxygen/nitrogen analyzer (TC-436, LECO Co., St. Joseph, MI, USA). The sintering aids are Y_2O_3 (purity of >99.9%, Shin-Etsu Chemical Co. Ltd., Tokyo, Japan), $MgSiN_2$ (0.63 wt.% O, 33.01 wt.% N, synthesized in our laboratory) and Li_2CO_3 (purity of >99%, Kojundo Chemical Lab, Saitama, Japan). The compositions of Si compacts with sintering additives were determined based on the designed compositions of the RBSN materials after full nitridation as shown in Table 2. The Si powder was mixed with the sintering additives in methanol by planetary ball milling for 2 h in a Si_3N_4 jar with Si_3N_4 balls. The slurries were dried using a rotary evaporator at a temperature of 60 °C, subsequently dried at 110 °C in vacuum, and sieved through 100-mesh screen. About 18 g of powder mixture were uniaxially pressed in a 52 mm × 43 mm stainless steel die and then cold isostatically pressed at 300 MPa. Based on the apparent dimensions and weight, all Si compacts were determined to show a green density of $\sim$1.45 g cm^{-3} or $\sim$60% theoretical density (TD). Prior to nitridation, the Si compacts were cut in half. Thus, the Si green bodies used for nitridation had dimensions of approximately 48 mm × 20 mm × 6.5 mm. The Si green bodies were placed in a BN crucible with a BN powder (GP grade, Denki Kagaku Kogyo Co., Tokyo, Japan) bed and were nitrided in an alumina tube furnace with 1 l min^{-1} high-purity nitrogen flow at 1400 °C for 8 h. The nitrided samples were placed inside a triple-crucible arrangement, which consisted of inner double crucibles of BN and an outer graphite crucible. The BN powder was used only as a powder bed. The post-sintering was performed in a graphite resistance furnace (Multi-500, Fujidempa Kogyo Co. Ltd., Japan) at 1900 °C for 12 h under a nitrogen pressure of 1 MPa with heating and cooling rates of 10 °C min^{-1}.

It has been generally accepted that RBSN is formed through the following reaction:

$$3Si + 2N_2 = Si_3N_4. \quad (1)$$

According to reaction (1), the extent of nitridation is determined by the following equation:

Table 1a
Particle size distribution of the raw Si powders

Type	Particle size distribution[a]								Note[a]
A	Particle size (μm)	>45	>30	>20	>10	>5	>3	>1	<1	$d_{50} = 9.9$ μm
	%	2.8	7.3	14.9	25	18.8	5.6	8.1	17.5	
B	Particle size (μm)	>30	>20	>10	>5	>3	>1	>0.6	<0.6	$d_{50} = 1.4$ μm
	%	0	20	16.5	14.5	6.2	10.7	6.7	41	
C	Particle size (μm)	>45	<45							
	%	4.3	95.7							

[a] The data provided by the manufacturer.

Table 1b
Impurity element analysis of the raw Si powders

Type	Impurity element content (wt.%)				
	O[a]	Al	Ca	Fe	Mn
A	0.47	0.004	0.002	0.091	0.002
B	0.82	0.02	0.004	0.08	
C	0.55	0.26	0.12	0.4	

[a] All other data was provided by the manufacturer except that the oxygen contents were measured in this work.

$$\mathrm{EN} = \frac{3M_{\mathrm{Si}}\Delta W}{4M_{\mathrm{N}}m_{\mathrm{Si}}} \times 100\%, \tag{2}$$

where M_{S} and M_{N} are the atomic weights of silicon and nitrogen, respectively, and W and m_{Si} are the observed weight gain after nitriding and the weight of Si in the green compact before nitriding, respectively. Linear shrinkages were characterized by the apparent dimensional change of the samples during nitridation and post-sintering. Weight loss was determined by carefully measuring the weight of the samples before and after post-sintering. Bulk densities were measured by the Archimedes method in distilled water. Theoretical densities of fully nitrided materials or SRBSN were estimated based on the designed composition by the rule of mixture:

$$\rho_{\mathrm{th}} = \sum V_i\rho_i, \tag{3}$$

where ρ_i and V_i are the density and volume fraction of the ith phase, respectively. The density values used were 3.19 g cm^{-3} for Si_3N_4, 5.03 g cm^{-3} for Y_2O_3, 3.14 g cm^{-3} for $MgSiN_2$ and 2.01 g cm^{-3} for Li_2O. The relative density was given by the ratio of the bulk density and theoretical density. The phase composition was identified using X-ray diffractometry (XRD) (RINT 2500, Rigaku Co., Tokyo, Japan, Cu Kα radiation, 40 kV and 100 mA) on the cross-section of the nitrided and post-sintered materials. The quantitative analysis of α- and β-Si_3N_4 of the nitrided products was performed using the method described by Pigeon and Varma [22]. The microstructures of the nitrided bodies were characterized by SEM of the fracture surfaces. The post-sintered samples were polished with 1 μm diamond slurry, subsequently plasma-etched by CF_4 gas at 30 ml min^{-1} for 120 s in a commercial plasma etching apparatus (Model PR31Z, Yamato Scientific, Tokyo, Japan), and observed by SEM.

Disk specimens (10 mm diameter and 3 mm thick) for measuring thermal conductivity were prepared by grinding the SRBSN samples. The thermal diffusivity was measured by the laser-flash method (TC-7000, ULVAC, Yokohama, Japan). The thermal conductivity (κ) was calculated according to the equation:

$$\kappa = \rho C_p \alpha, \tag{4}$$

where ρ, C_p and α are the bulk density, specific heat and thermal diffusivity, respectively. A constant value of specific heat, 0.68 J g^{-1} K^{-1}, was used in this work [23]. To evaluate the mechanical properties, the bar specimens with dimensions of 3 mm × 4 mm × 40 mm were machined from the SRBSN materials, and finished using a No. 400 diamond wheel. Bending strength was determined by four-point bending with an inner span of 10 mm and an outer span of 30 mm under a cross-head speed of 0.5 mm min^{-1} at room temperature. Fracture toughness was determined by the single-edge-precracked-beam (SEPB) method at room temperature [20,24].

Table 2
Final composition after full nitridation

Sample	Composition (mol%/wt.%)				Theoretical density (g cm^{-3})
	Si_3N_4	Y_2O_3	$MgSiN_2$	Li_2O	
AYM	93/93.86	2/3.25	5/2.89		3.23
AYML1	91/93.32	2/3.30	5/2.94	2/0.44	3.22
AYML2	89/92.77	2/3.36	5/2.99	4/0.89	3.21
BYM	93/93.86	2/3.25	5/2.89		3.23
CYM	93/93.86	2/3.25	5/2.89		3.23
CYML	91/93.32	2/3.30	5/2.94	2/0.44	3.22

3. Results and discussion

3.1. Si powders

As shown in Table 1a, both powders A and C are coarse and powder B is fine. Correspondingly, powders A and C exhibit a similar oxygen content, which is higher than that of powder B, as shown in Table 1b. For these powders, there is a significant difference in the Al impurity content by one or two magnitudes: C > B > A. In addition, there are differences in the other metallic impurity contents (e.g. Ca and Fe) between these powders. Both powders A and B show similar levels of Ca and Fe impurities, which are much lower than those in powder C. As a result, powder A is the purest one, and powder C is the impurest one.

Fig. 1a–c shows the SEM micrographs of the as-received Si powders. All the powders show a very wide particle size distribution with irregular shapes, and they follow the sequence of the particle size: A > C > B. In powder A, the largest particles found are ~70 μm in size, in powder B, ~30 μm and in powder C, ~50 μm. Fig. 1d–f shows the SEM micrographs of the three powder mixtures obtained by planetary milling for 2 h. Clearly, the Si particles are significantly ground during milling. However, some particles as large as ~10 μm in size are still observed in all cases, as typically indicated by block arrows in Fig. 1d–f. The number of these large Si particles is highest in powder mixture A, and lowest in powder mixture B. Although particle size measurements after milling were not conducted in the present work, it is clear that the overall Si particle size in the mixtures still follows the sequence of A > C > B, as is the case before milling.

3.2. Nitridation

Table 3 shows the nitridation results of the Si compacts after treatment at 1400 °C for 8 h. All the samples show more than 95% nitridation. As shown in Fig. 2, XRD analysis reveals that no Si peaks are observed in all samples, suggesting complete nitridation under the present nitriding conditions. As shown in Table 3, sample BYM shows the highest β-phase content, which is double that of samples AYM and CYM. Sample CYM shows a slightly higher β-phase content than sample AYM. When Li_2O is added, the β-phase content exhibits the order AYML1 < AYM < AYML2 for the powder A case, whereas the β-phase content exhibits the order CYML > CYM for the powder C case. In the absence of Li_2O, the densities show the order BYM > CYM > AYM. Correspondingly, sample BYM shows the highest linear shrinkage of up to 1.49%, whereas samples AYM and CYM show a near "zero" linear shrinkage. In both coarse powder cases, the addition of Li_2O leads to a slight increase in the density: AYM < AYML1 < AYML2 and CYM < CYML. As shown in Fig. 2, in addition to the Si_3N_4 products, the crystalline secondary phases are also formed in all samples during the nitridation. In samples AYM, BYM and CYM, the $Y_2Si_3O_2N_4$ phase alone is observed. In samples AYML1, AYML2 and CYML, both the $Y_2Si_3O_2N_4$ and Li_2SiO_3 phases are observed. The formation of crystalline Li_2SiO_3 indicates that the evaporation of Li_2O is limited during the nitridation at 1400 °C [16], but the crystallization of Li_2SiO_3 should occur during the cooling state because of its low melting point of ~1200 °C [25]. However, no crystalline secondary phases related to the $MgSiN_2$ additive are

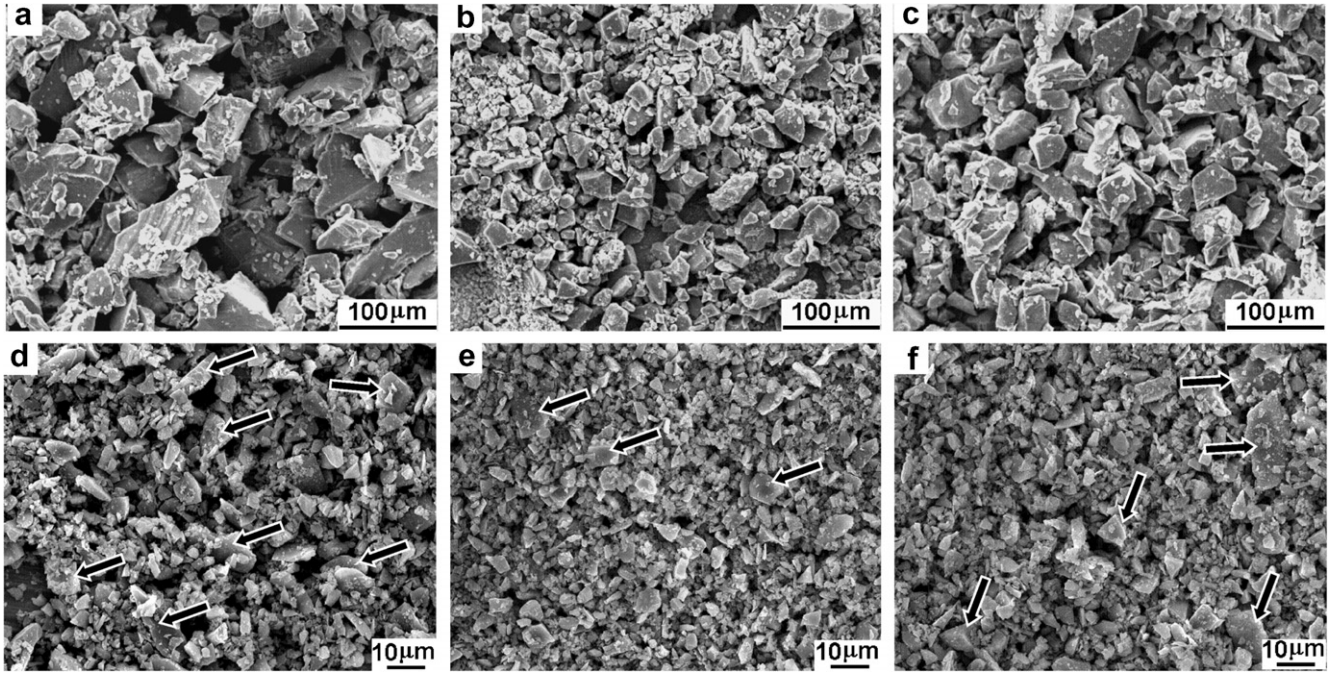

Fig. 1. SEM micrographs of the as-received Si powders: (a) A, (b) B and (c) C and the powder mixtures produced by planetary milling for 2 h: (d) AYM, (e) BYM and (f) CYM. Block arrows indicate the larger particles of ~10 μm.

Table 3
Nitridation results of the Si compacts after 1400 °C for 8 h

Sample	Nitridation (%)	β/(α + β) (wt.%)	Bulk density (g cm^{-3})	Relative density (%)	Linear shrinkage[a] (%)	Open porosity (%)
AYM	96.30	10.56	2.30	71.27	0.06	23.31
AYML1	96.52	4.50	2.32	72.19	0.77	24.62
AYML2	98.28	14.57	2.34	72.73	0.23	20.03
BYM	95.06	29.01	2.40	74.27	1.49	19.60
CYM	95.36	13.15	2.34	72.50	0.16	23.74
CYML	95.70	18.89	2.39	74.17	1.59	21.74

[a] The shrinkage along the radial direction.

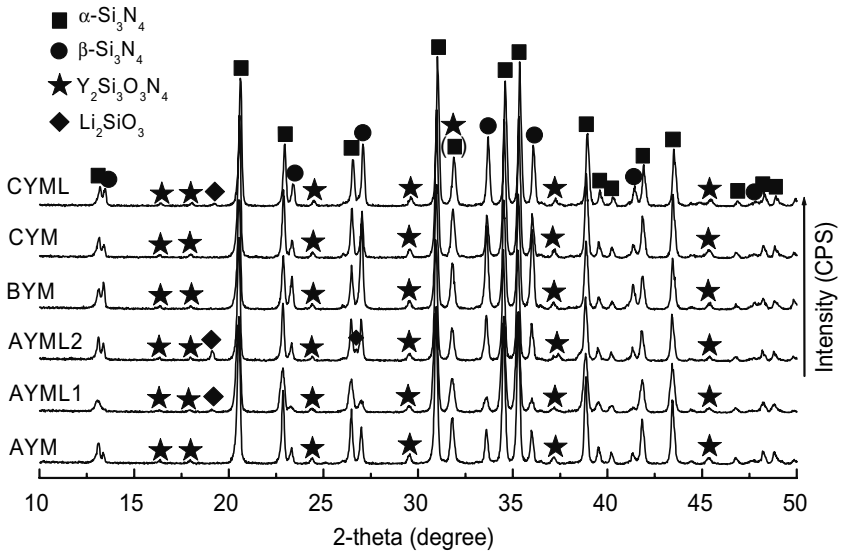

Fig. 2. XRD patterns of the samples nitrided at 1400 °C for 8 h.

observed in all samples, which is consistent with our previous findings [7,21], because the role of $MgSiN_2$ is to take part in the formation of a liquid phase during the nitridation. This seems to indicate that the lithium silicates devitrifies more easily than the magnesium silicates.

Fig. 3 shows the low-magnification SEM micrographs of the nitrided samples. It can be clearly seen that sample AYM shows the largest pore structure, containing a few large pores with a diameter of ~10 μm, as indicated by block arrows in Fig. 3a, whereas such large pores are barely observed in samples BYM and CYM. Compared with sample BYM, sample CYM has a greater quantity of large pores with a diameter of several micrometers, as typically indicated by the arrowheads in Fig. 3e. It is of interest to see that those large pores in sample AYM are no longer observed in sample AYML1, which has a rather uniform and finer porous microstructure. A similar phenomenon is also observed between samples CYM and CYML. Nevertheless, sample AYML2 shows a slightly coarser porous microstructure than sample AYML1 but still shows a finer porous microstructure than sample AYM. Generally, the nitridation reaction occurs by the nucleation and growth of Si_3N_4 on the clean surface of Si particles, resulting in the formation of a surface product layer. The reaction front then advances toward the center of the Si particle by nitrogen diffusing inward through the product layer and Si diffusing in vapor form to the reaction sites below the melting temperature (~1410 °C) of Si [26]. However, at the nitriding temperature of 1400 °C, the highly exothermic nitridation reaction allows some local temperatures to exceed the melting point of Si, so the unreacted large Si particles melt and penetrate into the surrounding porous nitride matrix by capillary forces, leaving large pores similar in size and shape to the particles, as observed in sample AYM.

Our previous work suggested that the Si_3N_4–Y_2O_3–SiO_2–$MgSiN_2$ system has a eutectic temperature of <1400 °C [7]. The incorporation of more oxygen or more metallic impurities leads to a reduction in the viscosity of the liquid phase. The Li_2O addition not only generates the Y–Si–Mg–Li–O–N liquid phase with lower viscosity but also contributes to forming a higher amount of the liquid phase. Therefore, it is expected that more of the less-viscous liquid phase fills the open pore channels in the surface nitride layers and surrounding nitride matrix to a greater extent, preventing the molten Si from penetrating into the surrounding matrix. The largest pore size in sample AYM is due to the largest Si particles and the highest purity. In contrast, the finest pore size in sample BYM is due to the finest Si particles and more oxygen, and the

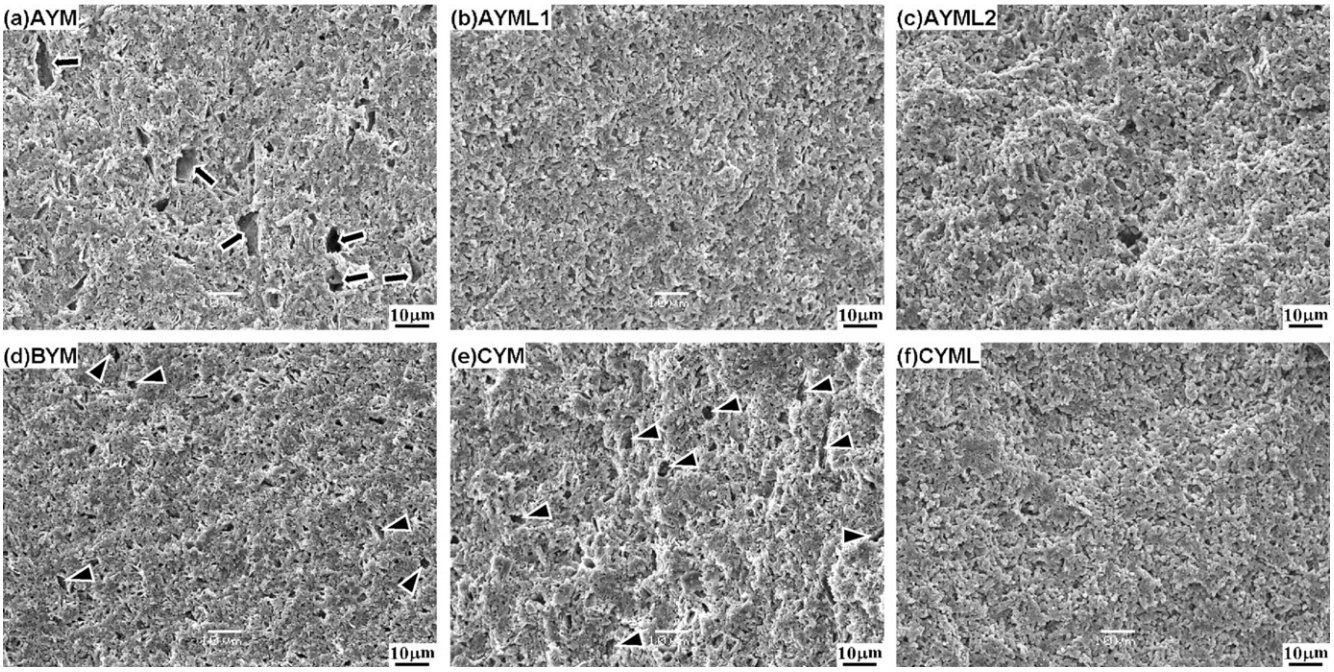

Fig. 3. Low-magnification SEM micrographs of fracture surfaces of the samples nitrided at 1400 °C for 8 h: (a) AYM, (b) AYML1, (c) AYML2, (d) BYM, (e) CYM and (f) CYML. Block arrows and arrowheads indicate the large pores with a diameter of ~10 μm and several micrometers, respectively.

finer pore size in sample CYM is mainly due to more of the metallic impurities. Moreover, due to the presence of more of the less-viscous liquid phase, Li_2O addition results in a more uniform and finer pore structure. In addition, the higher amount of the less-viscous liquid phase leads to an increased density. The present result further suggests an efficient technique for minimizing the largest pores in RBSN by the additive composition design, particularly for the case of coarse Si raw powders of several micrometers and even a few tenths of a micrometer in size [21]. This is advantageous for improving the properties of RBSN, such as strength and oxidation [27].

Fig. 4 shows high-magnification SEM micrographs of the nitrided samples. It is clear that most of the Si_3N_4 prod-

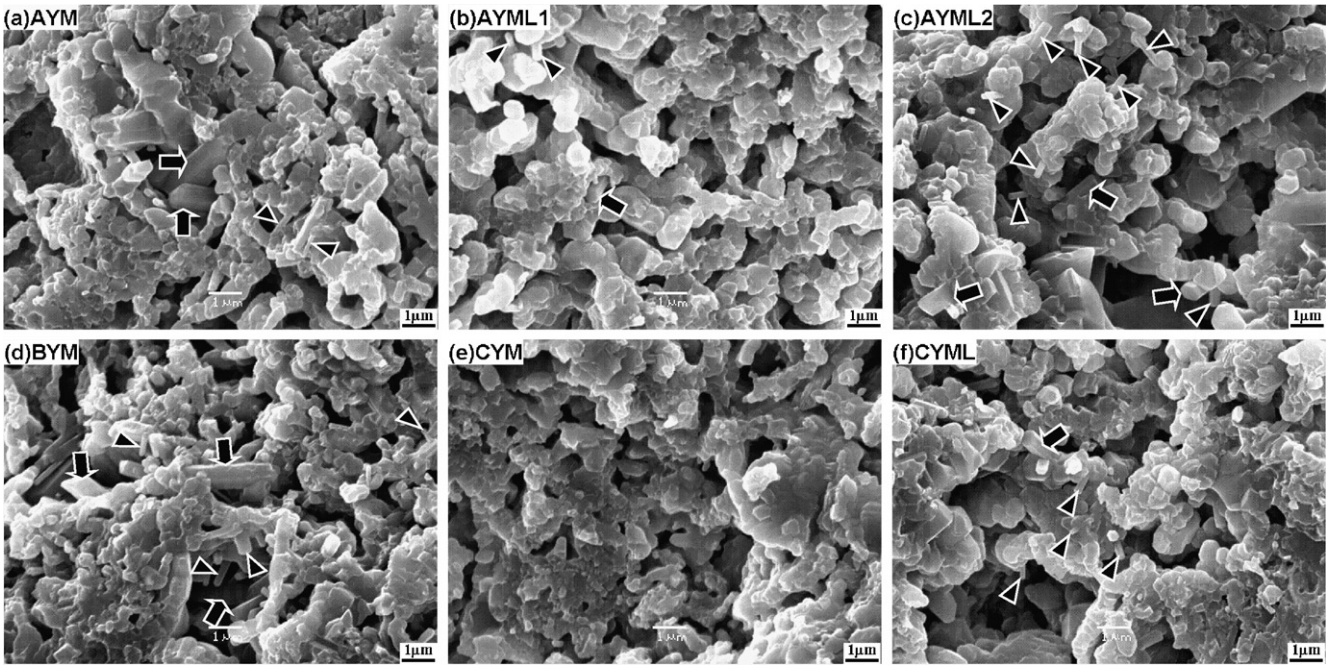

Fig. 4. High-magnification SEM micrographs of fracture surfaces of the samples nitrided at 1400 °C for 8 h: (a) AYM, (b) AYML1, (c) AYML2, (d) BYM, (e) CYM and (f) CYML. Block arrows and arrowheads indicate the coarse and fine rod-like β-Si_3N_4 grains with a radial diameter of ~1 μm and ≪1 μm, respectively.

ucts are fine and equiaxed in an agglomerated form in all samples, due to the major α-Si_3N_4 phase. However, some β-Si_3N_4 grains, typically characterized by a rod-like shape, are easily distinguished in the samples apart from in CYM, although sample CYM shows a higher β-Si_3N_4 content than sample AYM, as indicated by the block arrows and arrowheads (Fig. 4a–c and f), corresponding to the coarse and fine β-Si_3N_4 grains, respectively. It is not surprising that the rod-like β-Si_3N_4 grains are difficult to observe in sample CYM, because the β-Si_3N_4 grains also form in an equiaxed shape during the nitridation, similar to α-Si_3N_4 [28]. Some large β-Si_3N_4 grains of ~1 μm in radial diameter are found in samples AYM, AYML2 and BYM, particularly in AYM and BYM. No significant difference is found in the grain size of the α-Si_3N_4 product between samples AYM, AYML1 and AYML2, and between sample CYM and CYML. Nevertheless, sample BYM shows the overall finest α-Si_3N_4 product because it was made with the finest starting Si powder.

Many previous studies suggest that the β-Si_3N_4 grains grow preferably from the liquid phase by a nucleation and growth process through the dissolution–diffusion–precipitation process [29,30]. The growth of β-Si_3N_4 grains strongly depends on the characteristics of the liquid phase, including the chemical composition, viscosity and amount. The formation of large, rod-like β-Si_3N_4 grains is probably related to the less-viscous liquid phases, resulting in the faster mass transport of Si and N. As for sample AYM, the larger rod-like β-Si_3N_4 grain may be due to the higher amount of Si melt because of the large Si particles. However, sample AYM shows the lowest β-Si_3N_4 content in comparison with samples BYM and CYM. This is quite different from the previous findings that the larger Si particles tend to form more β-phase than the smaller Si particles [7,11,28]. In general, the β-phase formation is predominant during nitridation below the melting point of Si, but above this temperature the β-phase formation is predominant [26]. However, this is inconsistent with the present results, because the amount of molten Si should be higher in sample AYM than in sample BYM. The present result seems to further suggest that it is the characteristics of the individual liquid phase that control the formation of α- and β-phases during the nitridation of Si [31–33].

3.3. Post-sintering

XRD analysis reveals that the α–β phase transformation is complete in all samples during the post-sintering. In addition, the $Y_2Si_3O_3N_4$ phase alone is observed in all samples. Table 4 gives the post-sintering results after treatment at 1900 °C for 12 h. In the absence of Li_2O, due to the higher amount of liquid phase and finer nitride products, sample BYM attains nearly complete densification, showing a relative density of 99.9%. In contrast, due to insufficient liquid phase, samples AYM and CYM are densified to only ~87.8% and ~92% relative density, respectively. This is consistent with the highest shrinkage in sample BYM, compared with samples AYM and CYM. As shown in Fig. 5, the pores are barely present in sample BYM (Fig. 5d), but many pores several micrometers in size, and even greater than 10 μm, are present in samples AYM and CYM (Fig. 5a and e). Most of these pores are found to be isolated and closed pores, as also indicated by the open porosity data in Table 4.

When 2 mol% Li_2O is added, sample CYML is densified to 99.6% relative density, but sample AYML1 is densified to only 87.6% relative density, similar to sample AYM. As shown in Fig. 5, only a few pores are present in sample CYML (Fig. 5f), but a large number of pores is still present in sample AYML1 (Fig. 5b). However, when the amount of Li_2O is increased to 4 mol%, sample AYML2 is densified to ~100% relative density. This indicates that the Li_2O addition does enhance the densification of RBSN by providing more of the less-viscous liquid phase. As shown in Fig. 5c, only a few pores are present in sample AYML2. Evidently, the enhanced densification corresponds to the increase shrinkage: AYM < AYML1 < AYML2, and CYM < CYML. The results indicate that the densification of RBSN strongly depends on the characteristics of Si_3N_4 products and the amount of liquid phase rather than on the pore structure, which is consistent with our previous findings [7,21,34]. It is interesting to see that sample CYML contains a small number of large pores of several micrometers in size (Fig. 5f). Such large pores are not present in the nitrided body before post-sintering (Fig. 3f). This indicates that such large pores should be formed during the post-sintering. The results suggest that the fully dense SRBSN materials are preferably achieved in the RBSN that shows

Table 4
Linear shrinkage (LS), weight loss (WL), bulk density (BD), relative density (RD), open porosity (OP), thermal diffusivity (α), thermal conductivity (κ), bending strength (σ) and fracture toughness (K_{IC}) of sintered reaction-bonded Si_3N_4 materials (SRBSN) obtained at 1900 °C for 12 h under a nitrogen pressure of 1 MPa

Sample	LS (%)	WL (%)	BD (g cm^{-3})	RD (%)	OP (%)	α (cm^2 s^{-1})	κ (W m^{-1} K^{-1})	σ[a] (MPa)	K_{IC} (MPa $m^{1/2}$)
AYM	6.49	2.85	2.83	87.83	1.07	0.5318	102		
AYML1	6.85	5.15	2.82	87.60	1.54	0.4947	95		
AYML2	11.23	5.08	3.21	100.00	0.04	0.4942	108	538 ± 21 ($n = 3$)	8.9 ± 0.7 ($n = 3$)
BYM	9.74	2.69	3.22	99.92	0.17	0.5435	119	498 ± 16 ($n = 3$)	11.3 ± 1.1 ($n = 4$)
CYM	7.83	3.09	2.97	91.91	0.47	0.4181	84		
CYML	10.60	4.51	3.21	99.60	0.30	0.4266	93	693 ± 25 ($n = 3$)	10.2 ± 0.4 ($n = 3$)

[a] n is the number of specimens.

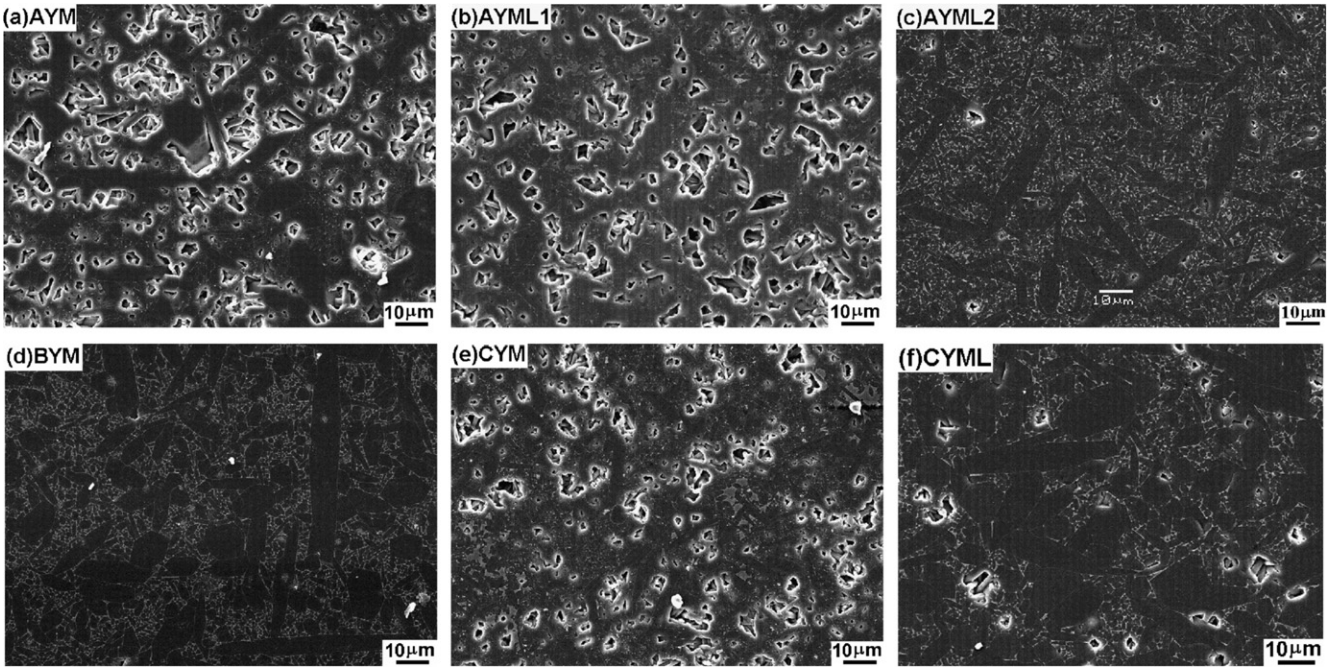

Fig. 5. SEM micrographs of polished and plasma-etched surfaces of the post-sintered material after treatment at 1900 °C for 12 h: (a) AYM, (b) AYML1, (c) AYML2, (d) BYM, (e) CYM and (f) CYML.

a finer pore structure, finer Si_3N_4 products and sufficient liquid phases, using fine-grained Si powder. In addition, sample BYM shows a lower weight loss than samples AYM and CYM, and the addition of Li_2O leads to an increased weight loss: AYML1 > AYM and CYML > CYM.

As shown in Fig. 5, it is clear that all samples exhibit a similar microstructure, composed of large, elongated β-Si_3N_4 grains surrounded by small matrix grains, particularly in the case of dense samples (Fig. 5c, d and f). In the absence of Li_2O, sample BYM shows the coarsest microstructure, composed of a higher fraction of larger elongated grains, but sample CYM shows the finest microstructure. Because sample BYM shows a substantially higher amount of β-Si_3N_4 than the other two samples before post-sintering, the reason for this should be related to the size of β-Si_3N_4 grains instead of the amount [35,36]. The pronounced large, elongated grain growth in sample BYM is attributed to the presence of larger rod-like β-Si_3N_4 grains during the nitridation (Fig. 4d). These large β-Si_3N_4 grains act as seed crystals and grow rapidly during the post-sintering by devouring neighboring small grains through the dissolution–reprecipitation process. Similarly, compared with sample CYM, the existence of large, rod-like β-Si_3N_4 seeds would allow sample AYM to exhibit a pronounced large, elongated grain growth. In the presence of Li_2O, the overall grain size follows the order of AYML2 > AYM > AYML1 for powder B and CYML > CYM for powder C. In these samples, the trend of the pronounced large, elongated grain growth seems to correlate well with the existence of large, rod-like β-Si_3N_4 seeds before post-sintering (Fig. 4). This further suggests that the size of β-Si_3N_4 nuclei in RBSN may play a dominant role in the microstructural evolution of SRBSN during the post-sintering [7,21,33]. Again, in dense samples, sample AYML2 shows the finest microstructure, and sample BYM shows the largest size and aspect ratio in the large elongated grains.

3.4. Thermal conductivity

Table 4 also shows the thermal diffusivity and thermal conductivity of all the SRBSB materials. Sample BYM has a thermal conductivity of 119 $W\,m^{-1}\,K^{-1}$, the highest value among all samples. Although sample AYM shows a thermal diffusivity close to that of sample BYM, the lower density leads to a substantially lower thermal conductivity in the former than in the latter. However, sample AYM shows substantially higher thermal diffusivity and higher thermal conductivity than sample CYM. Moreover, it is of interest to see that sample AYML1 shows a lower thermal diffusivity and thus lower thermal conductivity than sample AYM. Sample AYML2 shows almost the same thermal diffusivity as sample AYML1 but a higher thermal conductivity. Similarly, sample CYML shows a higher thermal conductivity than sample CYM, but the thermal diffusivity is similar between them.It should be noted that samples AYML2, BYM and CYML are dense, but samples AYM, AYML1 and CYM are porous. Porosity is known to lower the thermal conductivity of ceramics. Because most of the pores in samples AYM, AYML1 and CYM are closed and isolated, these materials can be regarded as a two-phase composite composed of the pores dispersed in a continuous solid matrix. If the thermal conductivity of

the pores is considered to be zero, the thermal conductivity of the composite, κ_c, can be described using Maxwell's equation [37]:

$$\kappa_c = \kappa_m \frac{2(1 - V_p)}{2 + V_p}, \quad (5)$$

where κ_m and V_p are the thermal conductivity of solid matrix and the volume fraction of the pores, respectively. Thus, the thermal conductivities of the solid matrix are estimated to be 124, 115 and 96 $W\,m^{-1}\,K^{-1}$ for samples AYM, AYML1 and CYM, respectively. The thermal conductivity without porosity is plotted as a function of the Al impurity content in Fig. 6a. It is evident that the thermal conductivity decreases as the Al impurity content increases, primarily due to the increased dissolution of Al in the β-Si_3N_4 lattice [4,8]. Compared with the Al impurity, the oxygen impurity seems less responsible for the difference in the thermal conductivities. In addition, the grain size effect is considered to be very limited, because the smallest grains reach nearly 1 μm in size [38]. It has been well documented that the dissolved O in β-Si_3N_4 can be removed during the sintering by using effective Al-free sintering additives, but the dissolved Al in β-Si_3N_4 is difficult to remove. Therefore, to enhance the thermal conductivity of β-Si_3N_4 ceramics, control of the Al impurity is of particular importance during the processing steps, e.g. the Al purity of the Si_3N_4 or Si raw powders is important.

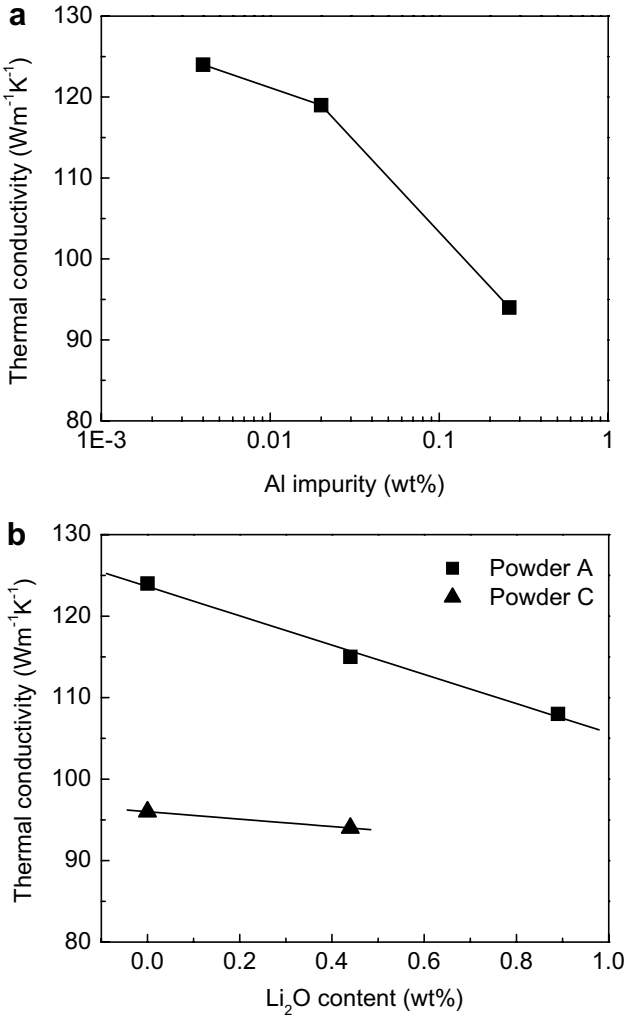

Fig. 6. Thermal conductivity as a function of (a) Al impurity and (b) Li_2O additive contents for SRBSN without porosity.

Fig. 6b also shows the thermal conductivity without porosity as a function of Li_2O content. It is found that the thermal conductivity maintains a linear decrease with increased Li_2O content, and the extent of decrease is larger for the purest powder A than for the impurest powder C. This indicates that the role of Li_2O in the thermal conductivity of β-Si_3N_4 is quite different from its role in the thermal conductivity of AlN, where the Li_2O addition contributes to the thermal conductivity not only by removing porosity but also by purifying the AlN grains [13,14]. Matovic's studies suggest that the remnant Li should be very limited in SRBSN obtained at 1900 °C for 12 h [16,19]. Because the Li_2O addition neither changes the amount of liquid phase nor dissolves in the β-Si_3N_4 lattice, the question arises: why does it lower thermal conductivity of SRBSN (β-Si_3N_4 ceramics)? Evidently, the effect of grain size can be excluded because the Li_2O addition leads to a larger grain size. This also suggests that the promoted grain growth would not guarantee the purification of β-Si_3N_4 grains via the dissolution–reprecipitation process; otherwise, the thermal conductivity should show an increase instead of a decrease.As observed in Fig. 5, the microstructure of the solid matrix without porosity is featured as follows: (i) on the first level, the solid matrix is composed of the glass pockets located at the triple grain-boundary junctions and a continuous matrix, and (ii) on the second level, the continuous matrix is composed of β-Si_3N_4 grains embedded in a continuous grain-boundary film. Based on the first-level microstructure, the thermal conductivity of the solid matrix, κ_m, can be described by Maxwell's equation [37]:

$$\kappa_m = \kappa_{ggf} \frac{2\kappa_{ggf}/\kappa_{glp} + 1 + 2V_{glp}(1 - \kappa_{ggf}/\kappa_{glp})}{2\kappa_{ggf}/\kappa_{glp} + 1 - V_{glp}(1 - \kappa_{ggs}/\kappa_{glp})}, \quad (6)$$

where κ_{ggf} and κ_{glp} are the thermal conductivities of the continuous matrix and glass pockets, respectively, and V_{glp} is the volume fraction of the glass pockets. Based on the second-level microstructure, the thermal conductivity of the continuous matrix, κ_{ggf}, can also be described by Maxwell' equation [37]:

$$\kappa_{ggf} = \kappa_{gbf} \frac{2 + \kappa_{SN}/\kappa_{gbf} + 2(1 - V_{gbf})(\kappa_{SN}/\kappa_{gbf} - 1)}{2 + \kappa_{SN}/\kappa_{gbf} - (1 - V_{gbf})(\kappa_{SN}/\kappa_{gbf} - 1)}, \quad (7)$$

where κ_{SN} and κ_{gbf} are the thermal conductivities of the β-Si_3N_4 grain and the grain-boundary film, respectively, and V_{gbf} is the volume fraction of the grain-boundary film. Again, the volume fraction of the grain-boundary film, V_{gbf}, can be given by Kitayama's equation [38]:

$$V_{gbf} = \delta\left(\frac{1}{w}+\frac{1}{l}\right)V_{SN}, \quad (8)$$

where w, l and V_{SN} are, respectively, the width, length and volume fraction of the β-Si_3N_4 grain, and δ is the grain-boundary film thickness.

According to Eqs. (6) and (7), Fig. 7 gives the thermal conductivity (κ_m) of the solid matrix (or SRBSN without porosity) as a function of the volume fraction of the grain-boundary film (V_{gbf}) and the isolated glass pockets (V_{glp}). Fig. 7a reveals that the thermal conductivity of SRBSN decreases with the increased amount of the grain-boundary film, but the extent of the decrease is larger in the case of β-Si_3N_4 grains with a higher thermal conductivity. Fig. 7b reveals that the thermal conductivity of SRSN decreases with the increased amount of the glass pockets, but it is less affected by the thermal conductivity of the glass pockets regardless of the thermal conductivity of the β-Si_3N_4 grains. Assuming that the grain-boundary film thickness is ~1 nm, a typical value in equilibrium for

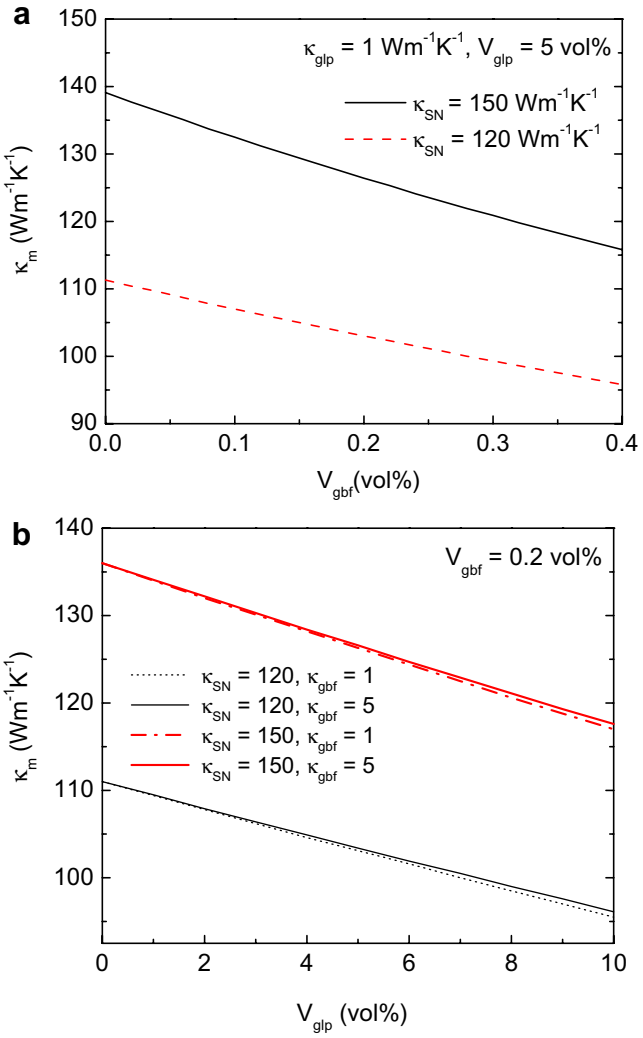

Fig. 7. Effects of (a) grain-boundary film and (b) isolated glass pocket on the thermal conductivity of SRBSN without porosity, calculated based on the Maxwell model.

β-Si_3N_4, the volume fraction of the grain-boundary film decreases with the increased grain size when the volume fraction of β-Si_3N_4 grain remains constant, as indicated by Eq. (8). Because Li_2O is removed in the vapor from the microstructure during the post-sintering, it is reasonable to assume that the Li_2O addition does not change the amount of the secondary phases or of the β-Si_3N_4 grains. Because the Li_2O addition eventually leads to a larger grain size, the grain-boundary film plays no role in the thermal conductivity. Although Li does not dissolve in the β-Si_3N_4 lattice, the Li_2O evaporation affects the sintering atmosphere in the closed BN crucible (porous). This very likely suppresses the removal of the lattice oxygen, thereby lowering the thermal conductivity [39]. In addition, it is not surprising that the Li_2O addition leads to a larger reduction in thermal conductivity with the increased purity of the Si powder, because the purer β-Si_3N_4 grain is more sensitive to the impurity in comparison with the impurer one. Therefore, the reason why the Li_2O addition leads to a reduction in thermal conductivity is most likely related to the increased number of crystal defects, typically such as lattice oxygen. Finally, it can be concluded that as a third disappearing additive, the negative effect of Li_2O on the thermal conductivity of SRBSN is not related to the Al impurity in the Si powder.

3.5. Mechanical properties

Table 4 also shows the bending strength and fracture toughness of dense SRBSN materials. It is found that sample BYM has the lowest bending strength and highest fracture toughness; this is in good agreement with the microstructure, which exhibits the highest fraction of larger elongated grains with a higher aspect ratio. The large, elongated grains act as reinforcing grains to increase fracture toughness by triggering crack bridging and crack deflection mechanisms [40]. In addition, they also probably act as larger structural flaws to reduce bending strength [41,42]. Sample AYML2 has the lowest fracture toughness, and its bending strength is slightly higher than that of sample BYM but substantially lower than that of sample CYML. The lowest fracture toughness seems to be consistent with the finest microstructure in sample AYML2. However, sample CYML shows the highest bending strength of up to 700 MPa, retaining the fracture toughness of up to 10.2 MPa $m^{1/2}$, although it shows a coarser microstructure than sample AYML2. One reason for this could be that sample CYML exhibits a higher fracture toughness than sample AYML2, because the higher toughness can allow ceramic materials to have higher tolerance to flaws [43]. However, despite the higher fracture toughness, sample BYM shows a much lower bending strength than sample CYML because of the largest elongated grains. The mechanical properties of Si_3N_4 ceramics depend not only on the grain morphology but also on the secondary phase chemistry. Satet et al. [44] showed that the weaker grain-boundary results in a higher toughness, but in a decreased

strength of the bulk materials. Becher et al. [45] reported that the interfacial strength is promoted by increasing the Al/Y and N/O ratios in the glassy phase. The highest strength in sample CYML, then, may also be due to the strongest interfacial strength because of the highest Al impurity and lower oxygen levels. Previous studies also reported that the lower-purity Si powder leads to a higher room-temperature bending strength than the higher-purity Si powder [6,46,47]. Although the higher metallic impurity levels lead to a degradation in the high-temperature strength, they also lead to a higher threshold stress to the creep-assisted crack growth process because of the higher fracture toughness [47]. Because the residual pores of several micrometers in size are more pronounced in sample CYML than in samples AYML2 and BYM, this seems to indicate that these pores are less important than other flaws as the fracture origins. From the commercial point of view, this work implies that, using the Y_2O_3–$MgSiN_2$ additive system, the low-purity coarse Si powder (such as powder C) is the most attractive one for developing SRBSN materials, because it possesses not only the lowest production cost but also a better compromise between thermal conductivity, bending strength and fracture toughness.

5. Conclusions

1. The addition of Li_2O allows coarser Si powders to produce a more uniform and finer pore structure by providing more of the less-viscous liquid phase, but the pore structure plays a less important role in the post-densification of RBSN in comparison with the characteristics of the liquid phase.
2. The purer fine Si powder leads to the fully densified SRBSN that does not require the addition of Li_2O, and the purest coarser Si powder requires a higher amount of Li_2O to produce nearly dense SRBSN materials than does the impurest coarse one.
3. The thermal conductivity of SRBSN without porosity decreases with increased Al impurity content and also decreases with the addition of Li_2O regardless of the Al impurity in the Si powders. However, the Li_2O addition leads to a larger decrease in the thermal conductivity with increased purity of the Si powder.
4. The impurest coarse Si powder leads to the lowest thermal conductivity (93 $W\,m^{-1}\,K^{-1}$) in SRBSN but to the highest four-point bending strength (~700 MPa) and a higher fracture toughness (~10 $MPa\,m^{1/2}$). In contrast, the purer fine Si powder leads to the highest thermal conductivity (119 $W\,m^{-1}\,K^{-1}$) and highest fracture toughness (~11 $MPa\,m^{1/2}$) but to the lowest bending strength (~500 MPa).

References

[1] Riley FL. J Am Ceram Soc 2000;83:245.
[2] Haggerty JS, Lightfood A. Ceram Eng Sci Proc 1995;16:475.
[3] Hirao K, Watari K, Brito ME, Toriyama Kanzaki MS. J Am Ceram Soc 1996;79:2485.
[4] Hirao K, Watari K, Hayashi H, Kitayama M. MRS Bull 2001;26:451.
[5] Mangels JA, Tennenhouse GJ. Am Ceram Soc Bull 1980;59:1216.
[6] Tiegs TN, Kiggans JO, Ploetz ZL. Ceram Eng Sci Proc 1993;14:378.
[7] Zhu XW, Zhou Y, Hirao K, Lenčéš Z. J Am Ceram Soc 2006;89:3331.
[8] Hirosaki N, Okamoto, Ando YM, Munakata F, Akimune Y. J Am Ceram Soc 1996;79:2878.
[9] Kitayama M, Hirao K, Tsuge A, Watari K, Toriyama M, Kanzaki S. J Am Ceram Soc 2000;83:1985.
[10] Kleebe HJ, Wötting G, Ziegler G. Sci Ceram 1988;14:407.
[11] Lee JS, Mun JH, Han BD, Kim HD, Shin BC, Kim IS. Ceram Int 2004;30:965.
[12] Hirosaki N, Ogata S, Kocer C, Kitagawa H, Nakamura Y. Phys Rev B 2002;65:134110.
[13] Watari K, Hwang HJ, Toriyama M, Kanzaki S. J Mater Res 1999;14:1409.
[14] Qiao L, Zhou HP, Chen KX, Fu RL. J Eur Ceram Soc 2003;23:1517.
[15] Matovic B, Rixecker G, Aldinger F. J Eur Ceram Soc 2004;24:3395.
[16] Matovic B, Rixecker G, Aldinger F. J Am Ceram Soc 2004;87:546.
[17] Jack KH. J Mater Sci 1976;11:1135.
[18] Tanaka I, Koichi K, Nasu S, Adachi H. J Am Ceram Soc 1993;76:2833.
[19] Matovic B. PhD dissertation, Max-Planck-Institute for Metals Research and University of Stuttgart, Stuttgart, Germany; 2003.
[20] Zhu XW, Hayashi H, Zhou Y, Hirao K. J Mater Res 2004;19:3270.
[21] Zhu XW, Zhou Y, Hirao K, Lenčéš Z. J Am Ceram Soc 2007;90:1684.
[22] Pigeon RG, Varma A. J Mater Sci Lett 1992;11:1370.
[23] Hayashi H, Hirao K, Toriyama M, Kanzaki S, Itatani K. J Am Ceram Soc 2001;84:3060.
[24] Nose T, Fujii T. J Am Ceram Soc 1988;71:328.
[25] Kracek FC. J Phys Chem 1930;34:2641.
[26] Moulson AJ. J Mater Sci 1979;14:1017.
[27] Ziegler G, Heinrich J, Wötting W. J Mater Sci 1987;22:3041.
[28] Heinrich J, Streb G. J Mater Sci 1979;14:2083.
[29] Mukerji J, Biswas SK. J Am Ceram Soc 1981;64:549.
[30] Shinozaki S, Milberg ME. J Am Ceram Soc 1981;64:382.
[31] Pavarajarn V, Kimura S. J Am Ceram Soc 2001;84:1669.
[32] Zhu XW, Zhou Y, Hirao K. J Am Ceram Soc 2004;87:1398.
[33] Zhu XW, Zhou Y, Hirao K. J Eur Ceram Soc 2006;26:711.
[34] Zhu XW, Zhou Y, Hirao K. J Mater Sci 2004;39:5785.
[35] Dressler W, Kleebe HJ, Hoffmann MJ, Rühle M, Petzow G. J Eur Ceram Soc 1996;16:3.
[36] Emoto H, Mitomo M. J Eur Ceram Soc 1997;17:797.
[37] Eucken A. Forsch Gebiete Ingenieurw B 1932;3:16.
[38] Kitayama M, Hirao K, Toriyama M, Kanzaki S. J Am Ceram Soc 1999;82:3105.
[39] Zhu XW, Sakka Y, Zhou Y, Hirao K. J Ceram Soc Jpn 2006;114:1093.
[40] Becher PF. J Am Ceram Soc 1991;74:255.
[41] Hirosaki N, Akimune Y, Mitomo M. J Am Ceram Soc 1993;76:1892.
[42] Kawashima T, Okamoto H, Yamamoto H, Kitamura A. J Ceram Soc Jpn 1991;99:320.
[43] Tajima Y, Urashima K. In: Hoffmann MJ, Petzow G, editors. Tailoring of mechanical properties of Si_3N_4 ceramics. Dordrecht: Kluwer; 1994. p. 101.
[44] Satet RL, Hoffmann MJ. J Am Ceram Soc 2005;88:2485.
[45] Becher PF, Sun EY, Hsueh CH, Alexander KB, Hwang SL, Waters SB, Westmoreland CG. Acta Mater 1996;44:3881.
[46] Tiegs TN, Kiggans JO, Montgomery FC, Lin HT, Barker DL, Snodgrass JD, et al. Ceram Eng Sci Proc 1996;17:354.
[47] Lin HT, Kiggans Jr JO, Tiegs TN. J Mater Sci 1996;31:6477.